Evidence for a Bubble-Competition Regime in Indirectly Driven Ablative Rayleigh-Taylor Instability Experiments on the NIF

D. A. Martinez, V. A. Smalyuk, J. O. Kane, A. Casner, S. Liberatore, and L. P. Masse

Evidence for a Bubble-Competition Regime in Indirectly-Driven Ablative Rayleigh-Taylor Instability Experiments on the NIF

D.A. Martinez, V.A. Smalyuk, J. O. Kane[1] and A. Casner, S. Liberatore, L. P. Masse[2]

[1]*Lawrence Livermore National Laboratory, Livermore, California 94550, USA*

[2]*CEA, DAM, DIF, F-91297 Arpajon, France*

(Dated: April 24, 2015)

Abstract

We investigate on the National Ignition Facility the ablative Rayleigh-Taylor instability in transition from weakly nonlinear to highly nonlinear regimes. A planar plastic package with pre-imposed two-dimensional broadband modulations is accelerated for up to 12 ns by the x-ray drive of a gas-filled Au radiation cavity with a radiative temperature plateau at 175 eV. This extended tailored drive allows a distance traveled in excess of 1 mm for a 130 μm thick foil. Measurements of the modulation optical density performed by x-ray radiography show that a bubble-merger regime for Rayleigh-Taylor Instability at an ablation front is achieved for the first time in indirect drive. The mutimode modulation amplitudes are in the nonlinear regime, grow beyond the Haan multimode saturation level, evolve toward the longer wavelengths and show insensitivity to initial conditions.

The Rayleigh-Taylor instability (RTI) [1] is the most well-studied hydrodynamic instability and occurs in many scientific and engineering scenarios, including two- component Bose-Einstein condensate [2], spray atomization in diesel engines [3], larger scale effects in geophysics [4] and supernovae explosions [5, 6]. The RTI occurs when a fluid accelerates another fluid of a higher density. A governing parameter is the nondimensional density difference or Atwood number $A_T = (\rho_1 - \rho_2) / (\rho_1 + \rho_2)$. This phenomenon may dramatically reduce the performance of inertial confinement fusion (ICF) experiments by degrading the symmetry of implosion [7]. the ablative RT instability growth is stabilized relative to classical RT during the linear stage, where the growth is exponential in time [8–10]. The self-consistent theory has shown a complicated dependence of the growth rate on the plasma parameters resulting in an Atwood number with a dependence on the wavenumber [11–13]. If the ablation front density is sharp leading to small density gradient scale length the Atwood number is close to unity for most of the wavenumbers of interest.

While growth in the linear regime of single-mode perturbations has been extensively studied [14–16] in both soft x-ray (inderect drive) and laser driven (direct drive) foils, the strongly nonlinear stage with broadband perturbations at an ablation front was only observed experimentally in laser driven foils [17]. Even the late-time dynamics of single-mode RTI is not trivial. Recent simulations have underlined the limitations of Layzer-type models[18] for the description of the nonlinear spike amplitude at any density ratio [19]. From an experimental point of view, few RTI experiments start from a well-prescribed initial state [20, 21]. Although previous studies on Omega used indirect drive to study the RTI these studies only accelerated the foil to a distance traveled of $450\mu m$ reaching only the weakly nonlinear regime for single mode modulations [16]. One major advantage of the experiments described below is the full knowledge of the initial surface perturbations (amplitude and phase) of a plastic solid foil vaporized and accelerated by the mass ablation induced by an intense x- ray flux. Furthermore, at an ablation front, the case where the Atwood number is near 1, a regime where computations and theory are challenged [22].

Good understanding of nonlinear growth of the RTI with broadband spectra is critical to thermonuclear ignition of ICF targets. Haan constructed a theory for the broadband RTI by comparing with classical interface without ablation [7], and his theory was first tested for an ablative interface driven by direct laser irradiation [17]. In comparison to direct drive, the ablation velocity and density gradient scale length are significantly increased
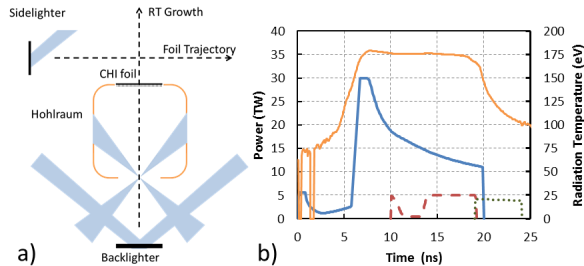
FIG. 1. (Color online) a) Experimental layout showing the half-hohlraum radiation cavity, back-lighter and side-lighter foils and the lasers driving these. b) Laser power vs. time (pulse shape) for the radiation drive (solid blue), backlighter (dashed red), and sidelighter (dotted green) x-ray sources. Overlapped is the measured radiation temperature from the x-ray flux diagnostic Dante (thin solid orange).

with indirect drive leading to cutoff wavelengths large enough, (about 20 microns) to be observable. For the first time we can measure the ablation front instability growth in a highly non-linear regime of the full unstable spectrum. Testing Haan theory and other theories [23–26] predicting increased bubble growth due to ablation in nonlinear regime are critical for ICF. This paper thus provides first test of the Haan theory for indirect drive in 2D planar geometry.

In this Letter, we investigate the strongly nonlinear evolution of the ablative RTI with a new indirect-drive platform. A distance traveled greater than $1\,mm$ is achieved for a $130\,\mu m$ thick planar plastic foil accelerated by a 20-ns long x-ray drive. We supply highly spatially resolved face-on radiographs which present the first evidence in indirect-drive of a bubble- merger regime for the RTI at an ablation front. By comparing RTI growth of a manufactured 2D broadband pattern with different initial amplitudes, the weak influence of initial conditions on final RTI growth is emphasized.

The experiments are performed with the National Ignition Facility (NIF) laser [27]. The experimental set-up is presented in Fig. 1a and detailed in Ref. [28]. A gold (Au) half-hohlraum is driven at one end by 60 NIF UV beams with a shaped laser pulse (Fig. 1b). The accelerated sample was a $130\,\mu m$ thick CH foil with a 0.6 % iodine dopant by atomic number with density of 1.2 g/cc, attached to the opposite end of the hohlraum. The hohlraum is gas-filled (room temperature neopentane at 400 torr) to delay wall plasma expansion in

order to keep a clear radiography line-of-sight at late time. The x-ray drive was measured through the laser entrance hole with Dante, a time-resolved, low resolution x-ray spectrometer consisting of 18 channels of filtered x-ray diodes [29] (Fig. 1b). A noticeable result is the flat temperature plateau at 175 eV created from 6 to 18 ns. This result is in accordance with two-dimensional radiation- hydrodynamics simulations of hohlraum energetics performed with FCI2 [30], taking into account M-band contributions determined with the Non Local Thermodynamical Equilibrium (NLTE) model Radiom [31].

The x-ray drive was cross checked with foil trajectory measurements using side-on radiography with a Vanadium x-ray backlighter. The sidelighter foil was heated with four NIF beams to create a $1\,mm$ diameter, 5 ns duration x-ray source. The driven foil was imaged using a pinhole array with $50\mu m$ diameter pinholes projected onto a four strip MCP gated x-ray detector (GXD) [32]. The position of the cold surface was measured using the 50% drop in intensity and the position of the surface with respect to the initial starting position of the foil was determined using a Au grid placed $1\,mm$ above the sample. After 20ns from the start of the laser pulse the foil was displaced 1.3 ± 0.05 mm from its initial position.

The growth of the ablative RTI was diagnosed using face-on radiography with a Vanadium area backlighter and imaged using a $10\mu m$ slit onto a four strip GXD and recorded with a CCD camera. To ensure that only the center region of the iodine doped CH sample was diagnosed, a 0.3x2 mm Au aperture was placed above the sample with the major axis oriented along the slit resolving direction. The backlighter foil was heated using two sets of eight NIF beams spaced 0.5mm apart to form a $1\,mm$ x $2\,mm$ elongated x-ray source aligned with the Au aperture. The intensity on the backlighter foil was $5 \times 10^{14} W/cm^2$. The photon energy of the x-ray source was determined using Al and Zn filter steps producing an equivalent monochromatic x-ray source of 6.3keV for the iodine doped CH foil due to He, Ly and continuum contributions to the backlighter spectrum.

The accelerated foil was machined with three modulation regions containing a well characterized 2D broadband modulation pattern (RMS = $2.8\,\mu m$) and two adjacent $\lambda = 50\mu m$ and $\lambda = 150\,\mu m$ sinusoidal modulations with a peak to valley of $0.5\,\mu m$. The 1mm wide broadband region consisted of a flat power spectrum with a $20\mu m$ wavelength cutoff (Fig. 3). The initial broadband RMS amplitude of $2.8\mu m$ was chosen to start near the saturation limit to maximize the nonlinear evolution of the ablative RTI. For comparison, a second sample was accelerated with the same machined multimode pattern but with smaller initial

4
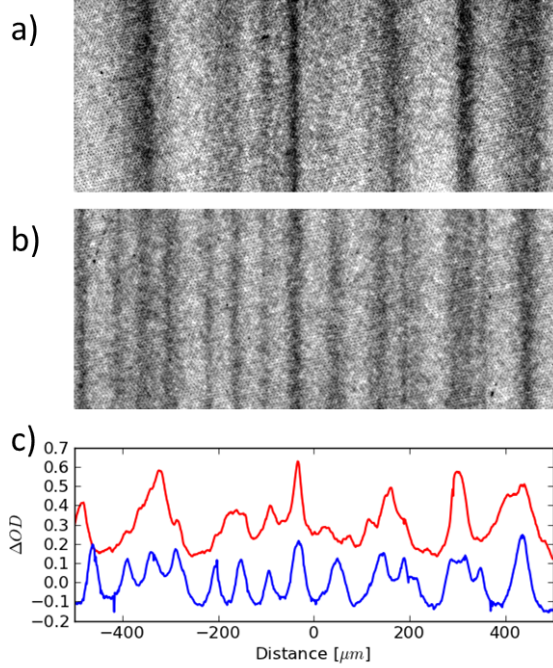
FIG. 2. (Color online) a) Processed data images at 15.5ns for iodine doped CH foil with initial RMS amplitude of $2.8\,\mu m$ where black represents an increase in optical density (OD). b) Data with an initial RMS amplitude of $0.5\mu m$. c) Lineouts from a) (red) and b) (blue). Red plot was shifted by $+0.3\Delta OD$ for clarity

amplitude (RMS $= 0.5\mu m$).

Radiography comparison between the two different amplitude samples is shown in Fig. 2 covering the 1mm broadband region at 15.5ns for 2.8 μm (Fig. 2a) and 0.5 μm (Fig. 2b) initial amplitude. Radiographs were converted to the deviation in optical density where the non-uniformity of the backlighter was subtracted using an 8th order polynomial fit[15] over the entire field of view to account for the two adjacent backlighter profiles. Shown in Fig. 2c are lineouts of the processed data at $15.5\,ns$ for both initial amplitudes. Similarities are observed between the two patterns highlighting the reproducibility of the machined modulations such as the large spikes at $x = +300\mu m$. Both lineouts exhibit the stereotypical "bubble and spike" morphology, however the RMS=$0.5\mu m$ initial amplitude case (Fig. 2b) shows 15 bubbles over the 1mm region while 11 bubbles are present in the $2.8\mu m$ initial RMS case suggesting that the larger amplitude initial spectrum is further along in the saturated regime. For determining nonlinear saturation we will investigate the broadband regions in
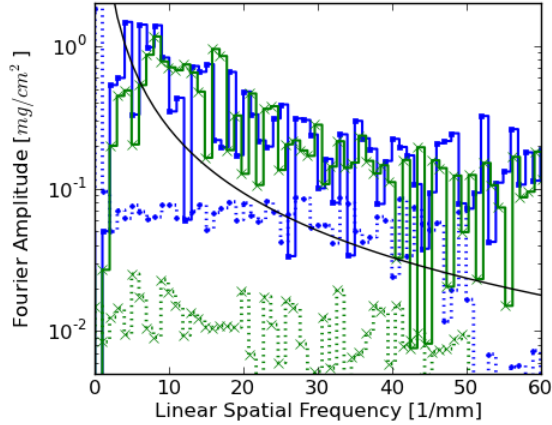
FIG. 3. (Color online) Comparing the absolute amplitude per mode of the broadband modulations at 15.5ns for initial amplitude RMS amplitude of 2.8 μm (blue steps with dots) and 0.5 (green 'x') overlapped with the Haan saturation limit for 2D broadband modulations (Black line) with $\rho = 1.2 g/cm^3$. The initial areal density amplitude spectrum is plotted as dotted lines with respective symbols and colors.

Fourier space.

For single mode modulations the RTI will grow exponentially until the amplitude is $\sim 0.1\lambda$, after which nonlinear effects become important. However, for a broad spectrum of Fourier modes, nonlinear saturation can occur earlier due to phase mixing of adjacent modes in Fourier space, as described by the Haan saturation model [33]. For 2D perturbations, the amplitude at which multimode saturation occurs is given by

$$S_{2D}(k) = \frac{1.13}{\sqrt{Lk^3}} \tag{1}$$

where k is the angular spatial frequency and L is the analysis box size. Taking the Fourier transform of the data at 15.5ns and correcting for the modular transfer function of the system[28] and converting to areal density we can compare to Eq. 1 taking into account the density of the foil at 15.5ns (Fig. 3). While initial modulation amplitudes are different by a factor of 5.6 the amplitudes are similar after significant nonlinear RT growth. This shows that the RT growth is insensitive to initial conditions. Both foils show similar amplitudes for $k > 10mm^{-1}$ regardless of the initial amplitude. The main difference in the spectrum is noticed for $k < 10mm^{-1}$ where $0.5\mu m$ initial RMS foil has a peak at $9mm^{-1}$ while the $2.8\mu m$ case has a peak at $4mm^{-1}$. Modes below the peak mode are in the linear regime and

6

differences in amplitude are noticeable. This low mode behavior is observed in the Fourier and in physical space as shown in Fig. 2 where Fig. 2a shows longer wavelength structure compared to the smaller initial amplitude foil (Fig. 2b). This behavior is predicted by the Haan saturation model [33, 34].

In the Haan saturation model the perturbations grow in the linear regime with the Takabe growth rate[8, 35]

$$\gamma(k) = \alpha\sqrt{\frac{gk}{1 + L_{min}k}} - \beta V_a k \tag{2}$$

where V_a is the ablation velocity, g is the acceleration, and L_{min} is the minimum density scale length. The amplitude of the perturbations from the linear model are described by $\xi_L(t, k) = a_0(k)\exp(\gamma(k)t)$, where $a_0(k)$ is the initial amplitude per mode. After the modulations reach the 2D Haan saturation limit the growth of the saturated mode grows linearly with respect to time

$$\xi(k, t) = S_{2D}(k)\left[1 + \log\left(\frac{\xi_L(k, t)}{S_{2D}(k)}\right)\right]. \tag{3}$$

Although the Haan model is an extension of the linear theory without higher order corrections, it serves as an illustration of the nonlinear behavior of the RTI in Fourier space.

The model was applied to the characterized modulation spectrum, ignoring the Richtmyer-Meshkov instability in order to illustrate the growth beyond the saturation limit. For this model the value for α and β were set to 1 which are consistent with previous x-ray driven ablative RTI work [36]. Typical values for β are between 1 and 3 with laser driven ablative RTI studies[10, 12, 37] reporting β values between 2.5-3.0. The other parameters, $V_a = 2.8\mu m/ns$, $L_{min} = 3.0\mu m$ and $g = 12.0\mu m/ns^2$ (Fig. 4) were obtained from 1D simulations. Comparison with the Haan model and the data is shown in Fig. 4 and produces reasonable agreement for both cases. Although the Haan model does not include all the relevant physics for ablative RTI, such as mode coupling [23–25], it is remarkable how that a simple models gives reasonable agreement with the data.

As the foil accelerates, the size of the RT features increases while larger bubbles overtake smaller bubbles. In order to illustrate this behavior the evolution of the perturbations is shown in Fig. 5 as a function of distance traveled, where the position of the interface was taken from 1D simulations and verified using side on radiography. The spatial size of the modulations was determined using the average density in a 50% peak density interval from 1D simulation and summarized in Table I. As the foil accelerates, the broadband
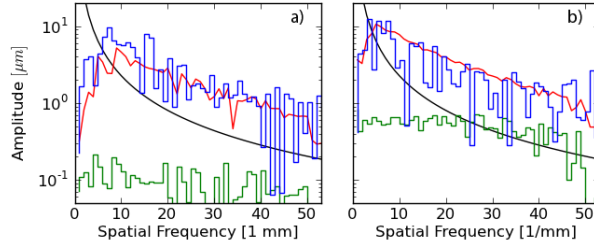
FIG. 4. (Color online) Amplitude per mode of the broadband region at 15.5ns (blue), Haan saturation amplitude (black) and the initial modulation spectrum (green) are shown for a) 0.5 μm RMS initial amplitude and b) 2.8 μm RMS initial amplitude. Overlapped with the data is the expected spectrum from the Haan model (red) from the initial spectrum.
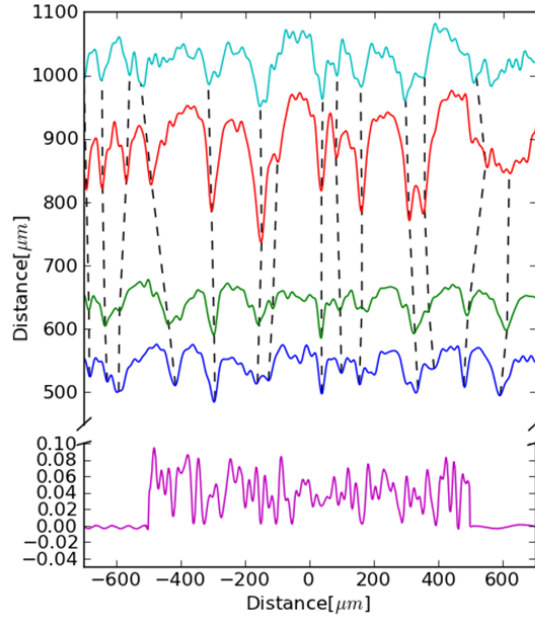
FIG. 5. (Color online) 2D Modulation evolution showing interface position at 14.5 (blue), 15.5 (green), 17.7 (red) and 18.7 ns (cyan). Dashed lines highlight the position of spikes as a function of time. Initial modulations are shown in the lower panel (magenta)

.

modulations are observed to expand and overtake smaller modulations. An illustration of the bubble expansion is also observed for modulations at $x = -400\ \mu m$ where the modulations initially start with a large bubble like structure. At 14.5ns the bubble is observed without the high frequency modulations and continually expands.

8

TABLE I. Broadband summary for RMS = 2.8 μm showing the RMS amplitude, density of the foil and distance traveled.

Time [ns]	RMS [g/cm^2]	ρ [g/cm^3]	Distance [μm]
0	0.322	1.2	0
14.5	0.159	1.28	544
15.5	1.78	1.20	642
17.7	4.37	1.05	893
18.7	2.03	0.98	1022

For nonlinear evolution, the RMS amplitude is expected to continually increase due to the cascade to lower modes. However, observations at 18.7ns show that the RMS amplitude decreases. This is caused by the bubbles perforating the foil. Once the target is punctured the bubbles will stop growing, producing a radiograph with reduced modulation growth later in time[14].

In summary, indirectly driven planar Rayleigh-Taylor experiments on NIF demonstrated that a radiation source is able to drive a foil into the strongly nonlinear regime. Using the Haan 2D saturation model (Eq. 1) both foils were beyond the saturation limit at 15.5ns for $\lambda < 100\,\mu m$. Comparing the growth from two different initial amplitudes at 15.5ns shows that the nonlinear regime of the RTI growth is weakly dependent on the initial amplitude. In addition, for the initial RMS = $2.8\mu m$ the progression of the foil showed expansion of the modulation up to 17.7ns, thus showing that the nonlinear ablative Rayleigh-Taylor instability does experience bubble competition and bubble merger.

———————

[1] D. Sharp, Physica D: Nonlinear Phenomena **12**, 3 (1984).

[2] K. Sasaki, N. Suzuki, D. Akamatsu, and H. Saito, Phys. Rev. A **80**, 063611 (2009).

[3] J. C. Beale and R. D. Reitz, Atomization and Sprays **9**, 623 (1999).

[4] E. Lev and B. H. Hager, Geophysical Journal International **173**, 806 (2008).

[5] W. H. Cabot and A. Cook, Nature Phys. 2 **2**, 562 (2006).

[6] O. Porth, S. S. Komissarov, and R. Keppens, MNRAS **443**, 547 (2014).

[7] S. W. Haan, Phys. Rev. A **39**, 5812 (1989).

[8] H. Takabe, K. Mima, L. Montierth, and R. L. Morse, Physics of Fluids (1958-1988) **28**, 3676 (1985).

[9] M. Modestov, V. Bychkov, R. Betti, and L.-E. Eriksson, Physics of Plasmas (1994-present) **15**, 042703 (2008).

[10] V. Bychkov, M. Modestov, and C. Law, Progress in Energy and Combustion Science **47**, 32 (2015).

[11] R. Betti, V. N. Goncharov, R. L. McCrory, P. Sorotokin, and C. P. Verdon, Phys Plasmas. **3**, 2122 (1996).

[12] V. V. Bychkov, S. M. Golberg, and M. A. Liberman, Physics of Plasmas (1994-present) **1**, 2976 (1994).

[13] J. Sanz, Phys. Rev. Lett. **73**, 2700 (1994).

[14] B. A. Remington, S. W. Haan, S. G. Glendinning, J. D. Kilkenny, D. H. Munro, and R. J. Wallace, Phys. Rev. Lett. **67**, 3259 (1991).

[15] J. P. Knauer, R. Betti, D. K. Bradley, T. R. Boehly, T. J. B. Collins, V. N. Goncharov, P. W. McKenty, D. D. Meyerhofer, V. A. Smalyuk, C. P. Verdon, S. G. Glendinning, D. H. Kalantar, and R. G. Watt, Physics of Plasmas (1994-present) **7**, 338 (2000).

[16] D. K. Bradley, D. G. Braun, S. G. Glendinning, M. J. Edwards, J. L. Milovich, and et al., Phys. Plasmas **14**, 056313 (2007).

[17] V. A. Smalyuk, O. Sadot, J. A. Delettrez, D. D. Meyerhofer, S. P. Regan, and T. C. Sangster, Phys. Rev. Lett. **95**, 215001 (2005).

[18] K. O. Mikaelian, Phys. Rev. E **78**, 015303 (2008).

[19] P. Ramaprabhu, G. Dimonte, P. Woodward, C. Fryer, G. Rockefeller, K. Muthuraman, P.-H. Lin, and J. Jayaraj, Physics of Fluids **24**, 074107 (2012).

[20] Z. Huang, A. De Luca, T. J. Atherton, M. Bird, C. Rosenblatt, and P. Carlès, Phys. Rev. Lett. **99**, 204502 (2007).

[21] J. White, J. Oakley, M. Anderson, and R. Bonazza, Phys. Rev. E **81**, 026303 (2010).

[22] G. Dimonte, P. Ramaprabhu, D. L. Youngs, M. J. Andrews, and R. Rosner, Phys. Plasmas

12, 056301 (2005).

[23] J. Sanz, J. Ramírez, R. Ramis, R. Betti, and R. P. J. Town, Phys. Rev. Lett. **89**, 195002 (2002).

[24] J. Garnier, P.-A. Raviart, C. Cherfils-Clérouin, and L. Masse, Phys. Rev. Lett. **90**, 185003 (2003).

[25] J. Garnier and L. Masse, Physics of Plasmas (1994-present) **12**, 062707 (2005).

[26] R. Betti and J. Sanz, Phys. Rev. Lett. **97**, 205002 (2006).

[27] E. Moses, R. Boyd, B. A. Remington, C. J. Keane, and R. Al-Ayat, Phys. Plasmas **16** (2009).

[28] A. Casner, V. A. Smalyuk, L. Masse, A. Moore, B. Delorme, D. Martinez, I. Igumenshchev, L. Jacquet, S. Liberatore, R. Seugling, C. Chicanne, H. S. Park, and B. A. Remington, High Energy Density Physics **9**, 32 (2013).

[29] E. L. Dewald, K. M. Campbell, R. E. Turner, J. P. Holder, O. L. Landen, S. H. Glenzer, R. L. Kauffman, L. J. Suter, M. Landon, M. Rhodes, and D. Lee, Rev. Sci. Instrum. **75**, 3759 (2004).

[30] G. P. Schurtz, P. D. Nicolai, and M. Busquet, Phys. Plasmas **7**, 4238 (2000).

[31] M. Busquet, Physics of Fluids B: Plasma Physics **5**, 4191 (1993).

[32] G. A. Kyrala, S. Dixit, S. Glenzer, D. Kalantar, D. Bradley, N. Izumi, N. Meezan, O. L. Landen, D. Callahan, S. V. Weber, J. P. Holder, S. Glenn, M. J. Edwards, P. Bell, J. Kimbrough, J. Koch, R. Prasad, L. Suter, J. L. Kline, and J. Kilkenny, Rev. Sci. Instrum. **81**, 10E316 (2010).

[33] S. W. Haan, Phys. Rev. A **39**, 5812 (1989).

[34] D. Ofer, U. Alon, D. Shvarts, R. L. McCrory, and C. P. Verdon, Phys Plasmas **3**, 3073 (1996).

[35] R. Betti, V. N. Goncharov, R. L. McCrory, and C. P. Verdon, Phys. Plasmas **5**, 1446 (1998).

[36] J. D. Lindl, P. Amendt, R. L. Berger, S. G. Glendinning, S. H. Glenzer, S. W. Haan, R. L. Kauffman, O. L. Landen, and L. J. Suter, Phys. Plasmas **11**, 339 (2004).

[37] H. Azechi, T. Sakaiya, S. Fujioka, Y. Tamari, K. Otani, K. Shigemori, M. Nakai, H. Shiraga, N. Miyanaga, and K. Mima, Phys. Rev. Lett **98**, 045002 (2007).